

PhyDrawGen: Physically Grounded Diagram Generation from Natural Language

Nafiul Haque* Syed Nazmus Sakib* Shifat E Arman†

Department of Robotics and Mechatronics Engineering, University of Dhaka

Abstract

Generating physics diagrams from text requires strict adherence to physical laws. While current generative models produce visually plausible outputs, they systematically hallucinate force vectors, ignore conservation laws, and violate geometric constraints. We present **PhyDrawGen**, a neuro-symbolic pipeline that decouples semantic scene understanding from physical constraint satisfaction. First, a large language model extracts a typed scene graph from the problem text. A deterministic solver then converts this graph into a Planar Straight-Line Graph (PSLG), encoding force balance, optical paths, and field topologies as exact geometric primitives. Finally, a fine-tuned Qwen-VL model implements a visually grounded propose-verify loop to iteratively correct any constraint violations. Evaluated on a benchmark of 1,449 problems spanning mechanics, optics, and electromagnetism, **PhyDrawGen** significantly outperforms GPT-5-image, Gemini 2.5 Flash, and Gemini 3 Pro, demonstrating robust physical accuracy even on unusual-object problems.

1 Introduction

Physics diagrams, free-body diagrams, ray-optics constructions, and electromagnetic field maps are formal visual arguments in which every arrow encodes a physical law, every angle encodes a geometric constraint, and every spatial relationship encodes an interaction governed by classical physics. A force arrow pointing in the wrong direction is not merely an aesthetic defect; it is a false physical claim. As such the generation of physically grounded scientific diagrams represents a frontier at the intersection of natural language understanding, structured reasoning, and constrained visual synthesis.

Though diffusion models are capable of producing photorealistic images (Rombach et al., 2022; Ramesh et al., 2022; Saharia et al., 2022; Ho et al., 2020) and spatially conditioned generation through adapters (Zhang et al., 2023; Mou et al., 2024; Ye et al., 2023) and grounding mechanisms (Li et al., 2023; Bar-Tal et al., 2023; Johnson et al., 2018), the noise-addition and denoising architecture of diffusion models is fundamentally ill-suited to tasks that require hard constraint satisfaction. The denoising process optimizes for perceptual plausibility under a learned prior, not for algebraic correctness under physical law. When applied to physics diagram generation, this manifests as systematic failure: diffusion models hallucinate force directions, place arrows at geometrically inconsistent angles, omit forces that conservation laws require, and conflate visually similar but physically distinct configurations such as static friction opposing motion versus kinetic friction during sliding.

Recent benchmarks have documented the remarkable ability of large language models (LLMs) and vision-language models (VLMs) to *solve* physics problems from diagrams (He et al., 2024; Xiang et al., 2025; Lu et al., 2022; Yue et al., 2024; Lu et al., 2024), demonstrating strong chain-of-thought reasoning over structured visual inputs. Furthermore, LLMs exhibit strong capabilities in structured extraction from natural language, as demonstrated by scene graph generation pipelines (Gao et al., 2024) and spatial reasoning systems (Li et al., 2023). Crucially, chain-of-thought prompting (Wei et al., 2022; Kojima et al., 2022) enables LLMs to decompose physics problems into typed entities and relationships — objects, surfaces, physical actions, forces, and geometric constraints — in a form that is amenable to downstream constraint solving. We leverage this capacity in the opposite direction: rather than parsing a diagram to solve a problem, we parse a problem to construct a diagram.

*Equal contribution.

†Corresponding author: shifatearman@du.ac.bd

Under review at EMNLP. This is a preprint of the submitted manuscript.

We propose **PhyDrawGen**, a pipeline that separates the semantic task of understanding a physics problem from the symbolic task of satisfying its physical constraints by employing an LLM as a structured scene graph extractor and a deterministic constraint solver as an exact physical verifier. The constraint solver produces a Planar Straight-Line Graph (PSLG) in which physical laws are encoded as typed geometric primitives that covers mechanics, optics, and electromagnetism under a single representational framework. The complete output is a standard physics diagram comprising a full scene with labeled force arrows and per-object free-body diagrams.

This approach addresses the discrepancy between probabilistic visual representations and structural physical laws. By transforming text into symbolic blueprints prior to rendering, we ensure semantic flexibility does not compromise geometric or physical truth.

We make three contributions:

1. **The PhyDrawGen scene graph schema.**

A typed heterogeneous graph whose CONSTRAINT node vocabulary maps directly to algebraic physical conditions. The schema covers mechanics, optics, and electromagnetism under a unified typed vocabulary of six node classes and six edge relations.

2. **The PSLG Constraint Solver.** A deterministic analytical solver that converts the scene graph into a Planar Straight-Line Graph encoding force balance, optical ray consistency, and field line topology as typed geometric constraint primitives.

3. **A Learned Constraint Correction Loop.**

A vision-language model fine-tuned via supervised learning on automatically generated constraint-violation examples, implementing a propose-verify correction loop that combines exact symbolic constraint checking with visually-grounded language model correction.

2 Related Work

Controlled synthesis and structured generation.

While diffusion models and spatial adapters have revolutionized text-to-image synthesis (Rombach et al., 2022; Ramesh et al., 2022; Saharia et al., 2022; Ho et al., 2020; Song et al., 2021; Zhang et al., 2023; Mou et al., 2024; Ye et al., 2023), they

inherently optimize for visual plausibility under a learned prior rather than hard symbolic constraints. Consequently, even with advanced layout grounding (Li et al., 2023; Bar-Tal et al., 2023) or sketch guidance (Xing et al., 2026; Vinker et al., 2022), these architectures cannot guarantee that generated force arrows or optical rays adhere to Newton’s or Snell’s laws. To enforce physical coherence, recent work has increasingly turned to structured intermediate representations. By conditioning synthesis on typed relational graphs (Johnson et al., 2018; Xu et al., 2017; Gao et al., 2024) and utilizing neuro-symbolic frameworks that decouple semantic reasoning from deterministic verification (Huang et al., 2026), systems can achieve robust constraint satisfaction. PhyDrawGen extends this paradigm; we leverage LLM chain-of-thought spatial reasoning (Li et al., 2023; OpenAI, 2023; Liu et al., 2023; Bai et al., 2023; Wei et al., 2022; Kojima et al., 2022) but replace general spatial semantics with a domain-specific vocabulary grounded strictly in classical physics.

Physics reasoning and diagram understanding.

The ability of vision-language models to reason over physics diagrams has been extensively benchmarked (He et al., 2024; Xiang et al., 2025; Lu et al., 2022; Yue et al., 2024; Lu et al., 2024), revealing strong chain-of-thought performance on diagram-based problem solving across mechanics, optics, and electromagnetism. These benchmarks establish that current models can *interpret* physics diagrams with high accuracy, yet the inverse capability which is *generating* physically correct diagrams from natural language has received minor attention. Physics education research has long documented that even advanced students who conceptually understand force and motion frequently fail to construct geometrically correct diagrams (Vignal and Wilcox, 2022; Hestenes et al., 1992). Translating conceptual understanding into geometric exactness requires a formal mathematical foundation. We draw on constrained quasiconformal mapping (Lai et al., 2026) and flat-foldability theory (Demaine and O’Rourke, 2007; Bern and Hayes, 1996; Hull, 2002), which establish a theoretical link between origami vertex closure and force balance, to build our PSLG constraint primitives. By integrating this rigorous geometric vocabulary, PhyDrawGen provides the first end-to-end framework that formalizes physics diagram generation as a structured prediction problem with

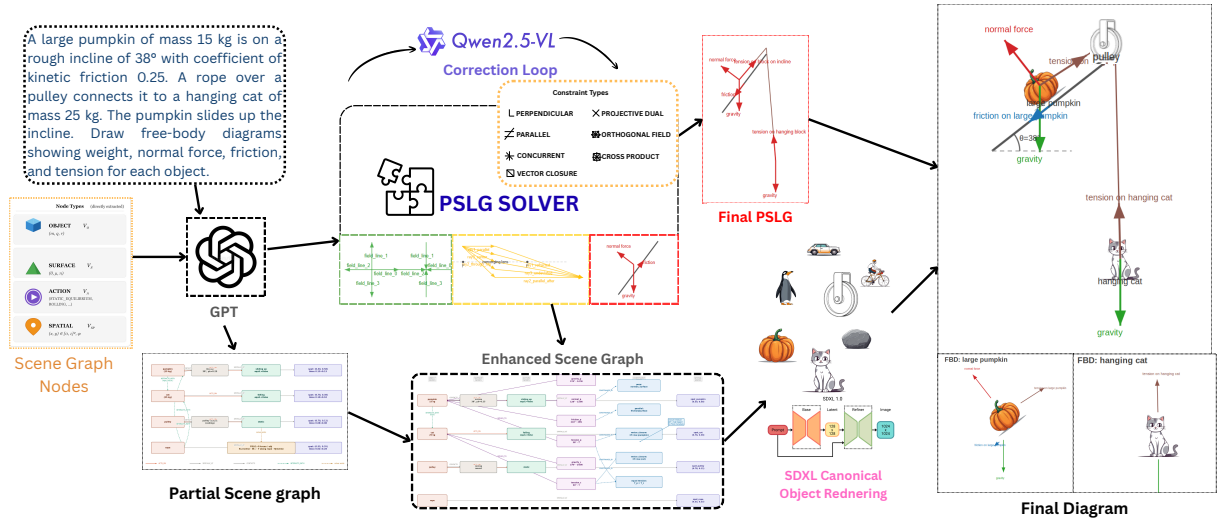


Figure 1: The overall pipeline of PhyDrawGen. To bridge semantic understanding and algebraic exactness, a language model (GPT-4o) extracts a typed scene graph from the text (left box). A solver converts it into a Planar Straight-Line Graph enforcing physical primitives (middle box), while a Qwen-VL loop iteratively corrects violations before rendering.

exact algebraic verification.

3 Methodology

3.1 Scene Graph Extraction

Given a physics problem text P , we extract a typed heterogeneous scene graph $\mathcal{G} = (\mathcal{V}, \mathcal{E})$ using GPT-4o with chain-of-thought self-checking (Wei et al., 2022; OpenAI, 2023). To structure the physical semantics, the node set \mathcal{V} is partitioned into six classes: OBJECT \mathcal{V}_O (mass, charge, radius), SURFACE \mathcal{V}_S (inclination, friction, refractive index), ACTION \mathcal{V}_A (e.g., STATIC_EQUILIBRIUM, ROLLING), FORCE \mathcal{V}_F (type, direction, normalized magnitude), SPATIAL \mathcal{V}_{Sp} (normalized 2D coordinates and orientation), and CONSTRAINT \mathcal{V}_C (explicit geometric conditions like PERPENDICULAR or VECTOR_CLOSURE). The edge set \mathcal{E} captures relations (ACTS_ON, CONTACTS, INTERACTS_WITH, APPLIES_TO, SPATIALLY_AT, CONSTRAINED_BY), each typed by domain $d \in \{\text{MECH, OPTICS, EM}\}$.

The LLM generates a partial graph $\mathcal{G}_{\text{LLM}} = (\mathcal{V}_{\text{LLM}}, \mathcal{E}, \delta)$, where $\mathcal{V}_{\text{LLM}} = \mathcal{V}_O \cup \mathcal{V}_S \cup \mathcal{V}_A \cup \mathcal{V}_{Sp}$ contains only the extractable entities, and δ maps edges to their physics domains. This extraction factors autoregressively over typed nodes (type τ_v , attributes \mathbf{a}_v) and edges τ_e . $p_\theta(\mathcal{G}_{\text{LLM}} | P) =$:

$$\prod_{v \in \mathcal{V}_{\text{LLM}}} p_\theta(\tau_v, \mathbf{a}_v | P) \prod_{(u, v, \tau_e) \in \mathcal{E}} p_\theta(\tau_e | u, v, P). \quad (1)$$

Extraction follows a rigorous five-step prompt sequence: (A) identify typed entities; (B) classify action states; (C) map inter-object contacts; (D) infer spatial positions; and (E) self-verify kinematic consistency (e.g., ensuring all FORCE nodes have targets and derivable normals). Crucially, the force and constraint sets ($\mathcal{V}_F, \mathcal{V}_C$) are not sampled by the LLM. Instead, they are instantiated deterministically by the downstream constraint solver conditioned on \mathcal{G}_{LLM} . The final graph is serialized as JSON and schema-validated before rendering.

3.2 PSLG Constraint Solver

Given \mathcal{G}_{LLM} , the solver produces a planar straight-line graph (PSLG) $\mathcal{H} = (\mathcal{P}, \mathcal{A}, \mathcal{C})$ — a typed straight-line embedding in $[0, 1]^2$ with vertex set \mathcal{P} , directed edge set \mathcal{A} carrying absolute angles $\theta_a \in [0, 2\pi)$, and geometric constraint set \mathcal{C} . Physical laws are encoded as typed constraint primitives, one per domain, derived analytically from the scene graph

Mechanics. For every OBJECT node o with action STATIC_EQUILIBRIUM, the solver enforces the vector closure condition

$$\sum_i \mathbf{F}_i = \mathbf{0}, \quad (2)$$

where the sum is over all force vectors applied to o . This is a CONCURRENT_STAR primitive: all force edges meet at the object centroid and their vector

sum closes (Demaine and O’Rourke, 2007). For a CONTACTS(o, s) edge with surface inclination θ , the normal force direction is constrained by

$$\hat{\mathbf{N}} \perp \hat{\mathbf{s}}, \quad \hat{\mathbf{s}} = (\cos \theta, \sin \theta), \quad (3)$$

the friction force direction satisfies $\hat{\mathbf{f}} \parallel \hat{\mathbf{s}}$ with sign determined by the direction of impending motion, and gravity is fixed at $\hat{\mathbf{g}} = (0, -1)$. For ROLLING objects, the torque constraint $\tau = f \cdot r = I\alpha$ is encoded as an additional CONSTRAINT node linking the friction force edge to the object radius. For non-equilibrium objects, Equation 2 is relaxed and the residual $\mathbf{F}_{\text{net}} = \sum_i \mathbf{F}_i \neq \mathbf{0}$ is emitted as an explicit net-force edge encoding the acceleration direction.

Optics. At each refracting interface, the solver enforces Snell’s law

$$n_1 \sin \theta_1 = n_2 \sin \theta_2, \quad (4)$$

where n_1, n_2 are the refractive indices from the SURFACE node and θ_1, θ_2 are the angles of incidence and refraction measured from the surface normal. For thin lenses, the solver computes the image position from the thin lens equation

$$\frac{1}{f} = \frac{1}{d_o} + \frac{1}{d_i}, \quad (5)$$

and encodes the incident parallel ray bundle and refracted convergent fan as a PROJECTIVE_DUAL primitive. At mirror surfaces, the reflection law $\theta_r = \theta_i$ is enforced as a CONSTRAINT node with type ANGLE_FIXED (Hecht, 2002).

Electromagnetism. For point charge interactions, the force on charge q_A due to charge q_B separated by displacement \mathbf{r} is directed along

$$\hat{\mathbf{F}}_{AB} = \text{sgn}(q_A q_B) \frac{\mathbf{r}}{|\mathbf{r}|}, \quad (6)$$

with sign enforcing attraction for opposite charges and repulsion for like charges (Griffiths, 2013). Field line edges are emitted as directed radial stars with edge count proportional to $|q|$, subject to the planarity constraint that no two field line edges cross, encoding Gauss’s law $\oint \mathbf{E} \cdot d\mathbf{A} = Q_{\text{enc}}/\epsilon_0$ (Griffiths, 2013). For Lorentz force problems, the force direction satisfies

$$\mathbf{F} = q(\mathbf{v} \times \mathbf{B}), \quad (7)$$

encoded as a CROSS_PRODUCT constraint node requiring $\mathbf{F} \perp \mathbf{v}$ and $\mathbf{F} \perp \mathbf{B}$ simultaneously. For

uniform fields, field line edges form a PARALLEL bundle with translational symmetry encoding $\nabla \times \mathbf{E} = 0$. The complete PSLG is verified against all active constraint nodes before rendering; any violation raises a solver exception and triggers the correction loop described in Section 3.4.

3.3 Enriched Scene Graph and Per-Object Canonical Rendering

Given the PSLG \mathcal{H} from Section 3.2, we derive an *enriched scene graph* \mathcal{G}_E from OBJECT_CORNER vertices of each object $o \in \mathcal{V}_O$ and recording its verified bounding box \mathbf{b}_o , centroid \mathbf{p}_o , and contact point \mathbf{c}_o ; this surfaces geometric quantities the solver has already fixed, no new information is introduced. To render each object the SVG renderer requires a label-specific canonical PNG that it embeds inside \mathbf{b}_o at the object’s PSLG orientation. This stage is fully label-driven and human-free: for every label ℓ_o in \mathcal{G}_E we strip qualifiers (*heavy, small, hanging, ...*) to a head noun $\tilde{\ell}_o$, slot it into a flat-illustration template $\phi(\tilde{\ell}_o)$, and draw N candidates from SDXL conditioned on that prompt, retaining the best by a connected-component filter $\{I_o^{(k)}\}_{k=1}^N \sim p_{\text{SDXL}}(\cdot | \phi(\tilde{\ell}_o))$. The final render object then becomes:

$$I_o^* = \arg \max_k \mathbb{1}[C(I_o^{(k)}) \geq \tau] s(I_o^{(k)}), \quad (8)$$

where $C(\cdot)$ is the largest-connected-component foreground ratio after REMBG background removal, $s(\cdot)$ is a silhouette quality score, and $\tau = 0.75$. The selected I_o^* is cached and reused by any later problem that mentions the same noun; a small set of primitive keys (POINT_MASS, ROPE, WIRE, POINT_CHARGE, SPHERE) is drawn procedurally with PIL instead, while every other label including unseen cases follow Eq. 8 on first use.

3.4 Constraint Correction via Supervised Fine-Tuning

Despite strong LLM extraction, scene graphs occasionally contain placement errors or missing relationships that propagate to constraint violations in the PSLG. We address this with a Qwen2.5-VL-3B-Instruct (Bai et al., 2023) correction model π_ϕ fine-tuned on automatically generated constraint-violation examples, implementing a propose-verify loop.

Training data generation. For each problem in the training set, we run the PSLG solver and record every constraint violation with its analytical correction. A violation instance is a tuple $(I_{\text{svg}}, \mathcal{G}, c, \Delta^*)$, where I_{svg} is the rendered SVG image, \mathcal{G} is the current scene graph JSON, c is a structured violation description, and Δ^* is the analytically derived correction patch. Correction patches are derived without human annotation: for a force balance violation with residual $\mathbf{r} = \sum_i \mathbf{F}_i \neq \mathbf{0}$, the correction adjusts the responsible force angle by $-\arg(\mathbf{r})$; for a normal direction violation, the correction sets $\theta_N = \theta_s + 90^\circ$; for a Snell violation, the correction recomputes θ_2 from Equation 4. This yields a training corpus derived entirely from the pipeline’s own failures, requiring no external annotation.

Training objective. The model is fine-tuned with LoRA adapters (Hu et al., 2021) to predict correction patches in a fixed JSON schema, minimising $\mathcal{L}_{\text{SFT}}(\phi) =$

$$\mathbb{E}_{(I, \mathcal{G}, c, \Delta^*) \sim \mathcal{D}} \left[- \sum_k \log \pi_\phi(\Delta_k^* | I_{\text{svg}}, \mathcal{G}, c, \Delta_{<k}^*) \right] \quad (9)$$

where Δ_k^* denotes the k -th token of the correction patch. The training signal is further structured by three physics-informed auxiliary losses. The closure loss

$$\mathcal{L}_{\text{closure}} = \left\| \sum_i \hat{\mathbf{u}}_i \right\|^2, \quad (10)$$

where $\hat{\mathbf{u}}_i$ is the unit vector in the direction of the i -th predicted force arrow, penalises deviations from vector closure at equilibrium vertices and is set to zero for non-equilibrium objects. The geometry loss

$$\mathcal{L}_{\text{geom}} = \sum_j \left\| \mathbf{p}_j - \mathbf{p}_j^* \right\|^2, \quad (11)$$

penalises deviation of each predicted attachment point \mathbf{p}_j from its physics-correct target \mathbf{p}_j^* derived from the SAM-detected object boundary. The relation loss

$$\mathcal{L}_{\text{rel}} = \sum_{e \in \mathcal{E}_{\text{contact}}} \left(\hat{\mathbf{N}}_e \cdot \hat{\mathbf{s}}_e \right)^2, \quad (12)$$

penalises deviation from the perpendicularity constraint in Equation 3 for each active contact edge. The total training loss is

$$\mathcal{L} = \mathcal{L}_{\text{SFT}} + \mathcal{L}_{\text{closure}} + \mathcal{L}_{\text{geom}} + \mathcal{L}_{\text{rel}}, \quad (13)$$

3.5 Evaluation Metrics

We use a single set of *neutral* ground-truth arrows, derived once per problem from the GPT-extracted scene graph \mathcal{G}_{LLM} and the problem text P via closed-form textbook physics formulas (catalogued in Appendix C.3). This ground truth is completely independent of the constraint solver. Let $\mathcal{A}^*(p) = \{(\theta_i^*, \ell_i^*)\}_{i=1}^{N_p}$ denote the neutral ground-truth set of angles and force labels for problem p , and let $\hat{\mathcal{A}}(p) = \{(\hat{\theta}_j, \hat{\ell}_j)\}_{j=1}^{\hat{N}_p}$ denote the predicted set (Hough segments or VLM-judged arrows, defined below). All three metrics use this same neutral $\mathcal{A}^*(p)$ and are scored at a tolerance threshold of $\tau = 10^\circ$ unless otherwise noted.

Hough-CSR. For each rendered diagram, we apply a Canny edge detector followed by the probabilistic HOUGHLINESP segment detector (Matas et al., 2000) to produce $\hat{\mathcal{A}}(p)$. A greedy minimum-angular-distance assignment matches each predicted segment to one ground-truth arrow within a 20° admissibility gate, yielding a matched set $\mathcal{M}(p)$. The binary **Hough-CSR** (Constraint Satisfaction Rate) metric for a problem is 1 if and only if every expected arrow is matched ($|\mathcal{M}(p)| = N_p$) and the maximum angular error among all matches is $\leq \tau$. We additionally report the mean angular error and the detection rate $|\mathcal{M}(p)|/N_p$ averaged across problems.

VCSR and LbCSR. A frozen VLM judge (Claude Opus 4.7) receives the rendered diagram alongside the problem text and is prompted to enumerate every visible arrow as a tuple $(\hat{\theta}_j, \hat{\ell}_j, \hat{o}_j)$ of angle, force-type label, and originating object. The judge’s output is parsed into $\hat{\mathcal{A}}(p)$ and Hungarian-matched (Kuhn, 1955) to the neutral ground truth $\mathcal{A}^*(p)$ under a composite cost $c_{ij} = \alpha \Delta \theta_{ij} + \gamma \mathbb{1}[\hat{\ell}_j \neq \ell_i^*]$. We report two binary problem-level metrics: the angle-only **VCSR**, which requires the maximum angular error of all matches to be $\leq \tau$, and the stricter **LbCSR**, which additionally requires exact label agreement ($\hat{\ell}_j = \ell_i^*$) for all matched pairs. Auxiliary statistics include the mean angular error and the label-match rate.

Blind judge. To isolate human-perceptible diagram quality, a separate frozen VLM (Claude Sonnet 4.6) is shown only the rendered diagram and the problem text P . It is prompted to evaluate six force categories $\mathcal{F} = \{\text{GRAVITY, NORMAL, FRICTION, TENSION, SPRING, APPLIED}\}$ assign-

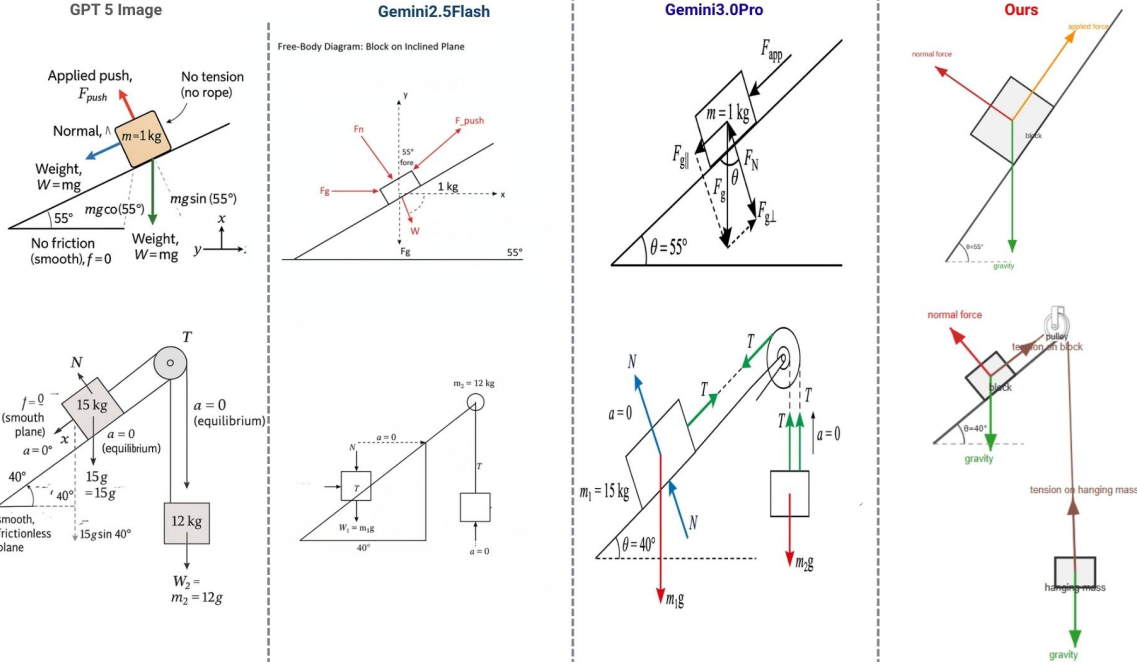


Figure 2: Qualitative comparison on standard mechanics problems. Each row shows the input problem, outputs from GPT-5-image, Gemini 2.5 Flash, Gemini 3 Pro, and PhyDrawGen (ours). Force arrows in baseline outputs frequently point in incorrect directions or violate equilibrium; PhyDrawGen arrows are derived analytically from the PSLG and satisfy all encoded constraints by construction.

ing each a verdict of CORRECT, WRONG, MISSING, or N/A. No solver output or ground truth is provided. The **Blind score** for a problem is simply the fraction of CORRECT verdicts out of all applicable categories (excluding N/A). We report the unweighted mean across the problem set, with per-category correctness rates broken out separately (see Appendix C.4 for the exact prompt and inter-judge sanity checks).

4 Experiments and Results

4.1 Experimental Setup

Implementation details. The full PhyDrawGen pipeline runs on a single NVIDIA RTX 4090 32 GB GPU. Scene graph extraction uses GPT-4o via API with temperature 0. The PSLG constraint solver and SVG renderer are deterministic and run in under one second per problem. The Qwen2.5-VL-3B-Instruct correction model is fine-tuned with LoRA adapters (Hu et al., 2021) for 16K iterations on the automatically generated violation dataset of 1.8k instances. Object rendering uses SDXL with Mistoline ControlNet (Zhang et al., 2023) at 1024×1024 resolution. Training the correction model requires 24–27 GB; inference for a complete diagram requires 6–9 GB.

Baselines. We compare against three state-of-the-art generative models: GPT-5-image, Gemini 2.5 Flash, and Gemini 3 Pro. All three are prompted directly with the problem text and asked to generate a physics diagram with labeled force arrows; no additional spatial conditioning or structured intermediate representation is provided.

4.2 Standard Textbook Problems

Method	H-V1	VCSR	LblCSR	Δ_{ang}	Blind
GPT-5-image	78.9%	79.7%	47.1%	2.2°	49.8%
Gemini 2.5 Flash	68.4%	73.7%	31.8%	3.0°	33.3%
Gemini 3 Pro	89.5%	57.9%	41.2%	3.6°	60.2%
Ours	78.9%	94.7%	77.9%	0.4°	65.8%

Table 1: Results on mechanics, optics, and electromagnetism problems. VCSR is the VLM-judged constraint satisfaction rate measuring geometric arrow correctness; LblCSR additionally requires correct force labels; Δ_{ang} is mean angular error in degrees; Blind is the blind VLM judge score. PhyDrawGen achieves the lowest angular error by 5x and the highest scores on all semantic and holistic metrics.

Table 1 reports results on problems across mechanics, optics, and electromagnetism problems. PhyDrawGen achieves 94.7% VCSR and 77.9% LblCSR, outperforming all baselines on both cor-

Method	Grv	Nrm	Frc	Tns	Spr	Apl
GPT-5-image	88%	65%	38%	86%	21%	100%
Gemini 2.5 Flash	72%	78%	17%	35%	78%	33%
Gemini 3 Pro	100%	78%	67%	100%	35%	60%
Ours	100%	90%	86%	60%	100%	70%

Table 2: Per-force-type blind judge scores mechanics subset. Grv: gravity. Nrm: normal. Frc: friction. Tns: tension. Spr: spring. Apl: applied. PhyDrawGen leads on four of six force types.

rectness metrics and reaching the highest blind judge score of 65.8%, above Gemini 3 Pro at 60.2%. The mean angular error of 0.4° is an order of magnitude lower than every baseline, confirming that PSLG-derived arrows are geometrically exact rather than approximately correct.

Table 2 breaks down blind judge scores by force type on the mechanics subset. PhyDrawGen achieves 100% on gravity and spring forces and leads on friction, consistent with the PSLG’s explicit enforcement of vertical gravity, surface-perpendicular normals, and surface-parallel friction directions. Tension and applied force scores are lower across all methods.

4.3 Open-Vocabulary Problems

Method	H-V1	VCSR	Lbl-CSR	Δ_{ang}	Blind
GPT-5-image	72.6%	46.2%	23.1%	4°	41.7%
Gemini 2.5 Flash	69.2%	61.5%	15.4%	3.6°	33.9%
Gemini 3 Pro	76.9%	53.8%	23.1%	2.7°	55.2%
Ours	76.9%	92.3%	73.8%	0.7°	53.6%

Table 3: Results on Open-Vocabulary-65, where physical objects are arbitrary real-world entities such as elephants, dogs, penguins, pumpkins, cyclists, rather than standard physics apparatus. PhyDrawGen leads on all objective metrics by a wide margin, demonstrating that constraint satisfaction generalises when object identity provides no implicit geometric prior. The blind judge gap versus Gemini 3 Pro reflects the latter’s stronger visual rendering of unusual objects.

Open-vocabulary problems probe a qualitatively different capability from standard textbook diagrams: the pipeline must generalise to objects e.g., elephants, watermelons, penguins, cartoon cats, cyclists that carry no implicit geometric prior about where forces should attach or in what direction they should point. A block on an incline always has a rectangular footprint; an elephant on the same incline does not, and no physics-specific training signal tells the model what an elephant looks like.

This set therefore directly tests whether physical constraint satisfaction is genuinely decoupled from object identity, which is the central architectural claim of PhyDrawGen.

Figure 3 shows qualitative outputs on three representative open-vocabulary problems; Table 3 reports quantitative results across the full set. PhyDrawGen achieves 92.3% VCSR against GPT-5-image’s 46.2%, a margin of more than 46 percentage points, and Label-CSR of 73.8% leads all baselines by a similarly large margin, confirming that force directions are derived from action and contact edges in the scene graph rather than from object identity. The blind judge score of 53.4% marginally lags Gemini 3 Pro’s 55.2%, a notable result given that Gemini produces visually richer scene synthesis. The objective correctness advantage is preserved even where our visual rendering of unusual objects is more schematic.

5 Ablation Studies

Condition	H-V1	VCSR	LblCSR	Δ_{ang}	Conv.
Clean GT (ceiling)	33.3%	68.0%	50.0%	1.6°	—
Perturbed (no SFT)	23.8%	48.8%	32.5%	5°	—
Perturbed + SFT	32.8	61.7	50.0	1.2°	78%

Table 4: Ablation: SFT recovery on 80 perturbed instances. **Conv.** is the fraction fully resolved within $T_{\text{max}}=5$ iterations. VCSR is the primary signal; Hough-V1 is noisy on this small mechanics-only set.

To evaluate the contribution of the Qwen-VL constraint-correction loop (Section 3.4), we construct a synthetic perturbation testbed of 80 held-out mechanics instances by applying two violation classes to clean GPT-4o-extracted scene graphs: **NORMAL-DIRECTION ERROR** (incline surface angle rotated by $\pm[12^\circ, 90^\circ]$) and **BBOX-PLACEMENT ERROR** (spatial node position shifted by $\pm[0.04, 0.25]$ on a random axis). We compare three conditions scored against the same neutral ground truth: **Clean GT** (unperturbed ceiling), **Perturbed (no SFT)** (perturbed scene graph rendered as-is), and **Perturbed + SFT** (perturbed graph corrected by the propose-verify loop with $T_{\text{max}}=5$). As reported in Table 4, removing the SFT loop drops VCSR by 19.2 pp ($68.0\% \rightarrow 48.8\%$) and raises mean angular error from 1.6° to 5° , confirming that perturbations propagate faithfully through the solver to the rendered diagram. The full pipeline with SFT recovers 12.9 pp of that gap,

misplaced force vectors, and conservation law violations prevalent in purely diffusion-based models.

Limitations

While PhyDrawGen successfully enforces hard physical constraints, its reliance on a deterministic, 2D Planar Straight-Line Graph (PSLG) restricts the framework to classical planar interactions, presenting an opportunity for future work to explore learned or dynamic constraint solvers capable of handling arbitrary 3D topologies. Furthermore, our evaluation benchmark is curated primarily from standard early-undergraduate physics curricula, omitting highly complex or abstract domains such as Olympiad-level mechanics or quantum phenomena (e.g., Feynman diagrams). Our baseline comparisons focus exclusively on state-of-the-art proprietary models (such as GPT-5-image and Gemini 3 Pro) because current open-weight generative models lack the zero-shot compositional text-to-image capabilities required to serve as meaningful, apples-to-apples baselines for this specific diagram-generation task. Finally, because the pipeline heavily depends on an initial LLM extraction, severely underspecified geometric parameters in the problem text can result in structural omissions that the downstream visual correction loop capped at $T_{\max}=5$ iterations cannot always resolve.

Ethics Statement

PhyDrawGen is intended to support physics education and the authoring of scientifically accurate teaching material; it generates diagrams from textbook-style problem statements and does not process personal, sensitive, or private data. Our evaluation benchmark is constructed from standard early-undergraduate physics problems and contains no human-subject information. The human-judge study reported in Appendix C.1 involved adult volunteers who participated voluntarily and anonymously, viewing only rendered diagrams and the accompanying problem text; no personal data was collected. The pipeline relies on a combination of proprietary APIs (e.g., GPT-4o) and open-weight models (Qwen2.5-VL, SDXL), each used in accordance with its respective terms of use. Finally, although our constraint solver enforces physical correctness by construction, generated diagrams may still contain residual errors; we therefore caution against treating the system as a sole authority

in safety-critical or assessment settings without expert review.

Acknowledgements

We thank Md Taif Islam Tonmoy and Muhammad Jiyad Hasan for their contributions to formulating the physical reasoning underlying this work, as well as for many valuable discussions on the representation and description of physics diagrams. Their feedback on the correctness of the mechanics, optics, and electromagnetism constructions was instrumental in shaping this paper.

Generative AI Usage

We used a generative AI assistant solely to aid manuscript writing, specifically for grammatical correction and minor stylistic polishing of author-written text. It was not used to generate research ideas, conduct experiments, or analyze results.

References

- Jinze Bai, Shuai Bai, Shusheng Yang, Shijie Wang, Sinan Tan, Peng Wang, Junyang Lin, Chang Zhou, and Jingren Zhou. 2023. [Qwen-VL: A versatile vision-language model for understanding, localization, text reading, and beyond](#). *arXiv preprint arXiv:2308.12966*.
- Omer Bar-Tal, Lior Yariv, Yaron Lipman, and Tali Dekel. 2023. [MultiDiffusion: Fusing diffusion paths for controlled image generation](#). In *International Conference on Machine Learning*, pages 1737–1752. PMLR.
- Marshall Bern and Barry Hayes. 1996. The complexity of flat origami. In *Proceedings of the Seventh Annual ACM-SIAM Symposium on Discrete Algorithms, SODA '96*, page 175–183, USA. Society for Industrial and Applied Mathematics.
- Erik D Demaine and Joseph O'Rourke. 2007. *Geometric Folding Algorithms: Linkages, Origami, Polyhedra*. Cambridge University Press, Cambridge, UK.
- Gege Gao, Weiyang Liu, Anpei Chen, Andreas Geiger, and Bernhard Schölkopf. 2024. [Graphdreamer: Compositional 3d scene synthesis from scene graphs](#).
- David J Griffiths. 2013. *Introduction to electrodynamics*. Pearson.
- Chaoqun He, Renjie Luo, Yuzhuo Wang, Jiannan Wang, Wei Chu, et al. 2024. [OlympiadBench: A challenging benchmark for promoting AGI with olympiad-level bilingual multimodal scientific problems](#). In *Proceedings of the 62nd Annual Meeting of the Association for Computational Linguistics*.

- Eugene Hecht. 2002. *Optics*, 4th intern edition. Addison Wesley.
- David Hestenes, Malcolm Wells, and Gregg Swackhamer. 1992. Force concept inventory. *The Physics Teacher*, 30(3):141–158.
- Jonathan Ho, Ajay Jain, and Pieter Abbeel. 2020. Denoising diffusion probabilistic models. In *Advances in Neural Information Processing Systems*, volume 33, pages 6840–6851.
- Edward J. Hu, Yelong Shen, Phillip Wallis, Zeyuan Allen-Zhu, Yuanzhi Li, Shean Wang, Lu Wang, and Weizhu Chen. 2021. Lora: Low-rank adaptation of large language models.
- Yanjia Huang, Yunuo Chen, Ying Jiang, Jinru Han, Zhengzhong Tu, Yin Yang, and Chenfanfu Jiang. 2026. Learn2fold: Structured origami generation with world model planning.
- Thomas C Hull. 2002. The combinatorics of flat folds: A survey. In *Origami³: Third International Meeting of Origami Science, Mathematics, and Education*, pages 29–38. A K Peters.
- Justin Johnson, Agrim Gupta, and Li Fei-Fei. 2018. Image generation from scene graphs. In *Proceedings of the IEEE Conference on Computer Vision and Pattern Recognition*, pages 1219–1228.
- Takeshi Kojima, Shixiang Shane Gu, Machel Reid, Yutaka Matsuo, and Yusuke Iwasawa. 2022. Large language models are zero-shot reasoners. In *Advances in Neural Information Processing Systems*, volume 35, pages 22199–22213.
- Harold W. Kuhn. 1955. The Hungarian Method for the Assignment Problem. *Naval Research Logistics Quarterly*, 2(1–2):83–97.
- Ka Ho Lai, Hei Tung Tsang, Gary P. T. Choi, and Lok Ming Lui. 2026. Optimization of constrained quasiconformal mapping for origami design.
- Yuheng Li, Haotian Liu, Qingyang Wu, Fangzhou Mu, Jianwei Yang, Jianfeng Gao, Chunyuan Li, and Yong Jae Lee. 2023. GLIGEN: Open-set grounded text-to-image generation. In *Proceedings of the IEEE/CVF Conference on Computer Vision and Pattern Recognition*, pages 22511–22521.
- Haotian Liu, Chunyuan Li, Qingyang Wu, and Yong Jae Lee. 2023. Visual instruction tuning. In *Advances in Neural Information Processing Systems*, volume 36.
- Pan Lu, Bansal Hritik, Tony Xia, Jiacheng Liu, Chunyuan Li, Hajishirzi Hannaneh, Cheng Hao, Chang Kai-Wei, Galley Michel, and Gao Jianfeng. 2024. MathVista: Evaluating mathematical reasoning of foundation models in visual contexts. In *International Conference on Learning Representations*.
- Pan Lu, Swaroop Mishra, Tanglin Xia, Liang Qiu, Kai-Wei Chang, Song-Chun Zhu, Oyvind Taffjord, Peter Clark, and Ashwin Kalyan. 2022. Learn to explain: Multimodal reasoning via thought chains for science question answering. In *Advances in Neural Information Processing Systems*, volume 35, pages 2507–2521.
- J. Matas, C. Galambos, and J. Kittler. 2000. Robust detection of lines using the progressive probabilistic hough transform. *Computer Vision and Image Understanding*, 78(1):119–137.
- Chong Mou, Xintao Wang, Liangbin Xie, Jian Zhang, Zhongang Qi, Ying Shan, and Xiaohu Qie. 2024. T2I-Adapter: Learning adapters to dig out more controllable ability for text-to-image diffusion models. In *Proceedings of the AAAI Conference on Artificial Intelligence*, volume 38, pages 4296–4304.
- OpenAI. 2023. GPT-4 technical report. *arXiv preprint arXiv:2303.08774*.
- Aditya Ramesh, Prafulla Dhariwal, Alex Nichol, Casey Chu, and Mark Chen. 2022. Hierarchical text-conditional image generation with CLIP latents. *arXiv preprint arXiv:2204.06125*.
- Robin Rombach, Andreas Blattmann, Dominik Lorenz, Patrick Esser, and Björn Ommer. 2022. High-resolution image synthesis with latent diffusion models. In *Proceedings of the IEEE/CVF Conference on Computer Vision and Pattern Recognition*, pages 10684–10695.
- Chitwan Saharia, William Chan, Saurabh Saxena, Lala Li, Jay Whang, Emily Denton, Seyed Kamyar Seyed Ghasemipour, Burcu Karagol Ayan, S. Sara Mahdavi, Rapha Gontijo Lopes, Tim Salimans, Jonathan Ho, David J Fleet, and Mohammad Norouzi. 2022. Photorealistic text-to-image diffusion models with deep language understanding.
- Jiaming Song, Chenlin Meng, and Stefano Ermon. 2021. Denoising diffusion implicit models. In *International Conference on Learning Representations*.
- Michael Vignal and Bethany R. Wilcox. 2022. Investigating unprompted and prompted diagrams generated by physics majors during problem solving. *Physical Review Physics Education Research*, 18(1).
- Yael Vinker, Ehsan Pajouhesh, Jessica Y Bo, Roman Hachohen, B Amit, Hadar Averbuch-Elor, Daniel Cohen-Or, and Ariel Shamir. 2022. CLIPasso: Semantically-aware object sketching. *ACM Transactions on Graphics (TOG)*, 41(4):1–11.
- Jason Wei, Xuezhi Wang, Dale Schuurmans, Maarten Bosma, Fei Xia, Ed Chi, Quoc V Le, and Denny Zhou. 2022. Chain-of-thought prompting elicits reasoning in large language models. In *Advances in Neural Information Processing Systems*, volume 35, pages 24824–24837.

Kun Xiang, Heng Li, Terry Jingchen Zhang, Yinya Huang, Zirong Liu, Peixin Qu, Jixi He, Jiaqi Chen, Yu-Jie Yuan, Jianhua Han, Hang Xu, Hanhui Li, Mrinmaya Sachan, and Xiaodan Liang. 2025. [Seep-hys: Does seeing help thinking? – benchmarking vision-based physics reasoning](#).

Ximing Xing, Chuang Wang, Haitao Zhou, Jing Zhang, Qian Yu, and Dong Xu. 2026. [Diffsketcher: Text guided vector sketch synthesis through latent diffusion models](#).

Danfei Xu, Yuke Zhu, Christopher B Choy, and Li Fei-Fei. 2017. [Scene graph generation by iterative message passing](#). In *Proceedings of the IEEE Conference on Computer Vision and Pattern Recognition*, pages 5410–5419.

Hu Ye, Jun Zhang, Sibao Liu, Xiao Han, and Wei Yang. 2023. [IP-Adapter: Text compatible image prompt adapter for text-to-image diffusion models](#). *arXiv preprint arXiv:2308.06721*.

Xiang Yue, Yuansheng Ni, Kai Zhang, Tianyu Zheng, Ruoqi Liu, Ge Zhang, Samuel Stevens, Dongfu Jiang, Weiming Ren, Yuxuan Sun, Cong Wei, Botao Yu, Ruibin Yuan, Renliang Sun, Ming Yin, Boyuan Zheng, Zhenzhu Yang, Yibo Liu, Wenhao Huang, Huan Sun, Yu Su, and Wenhao Chen. 2024. [Mmmu: A massive multi-discipline multimodal understanding and reasoning benchmark for expert agi](#).

Lvmin Zhang, Anyi Rao, and Maneesh Agrawala. 2023. [Adding conditional control to text-to-image diffusion models](#). In *Proceedings of the IEEE/CVF International Conference on Computer Vision*, pages 3836–3847.

A Additional Implementation Details

A.1 GPT Scene Graph Extraction

Stage 1 of the pipeline (Section 3.1) is implemented as a single GPT-4o call routed through OpenRouter with temperature 0. The model receives a system prompt that fixes the schema (six node classes, six edge classes, force / constraint node types reserved for the solver), a per-object bounding-box OBJECT-SIZE GUIDE with concrete anchors for unusual entities (elephant $\approx 0.30 \times 0.22$, cat / dog $\approx 0.10 \times 0.10$, wall $\approx 0.05 \times 0.60$, etc.), a five-step chain-of-thought scaffold (Steps A–E covering entities, actions, relationships, spatial layout, observed elements), and a *mandatory* self-check block that requires the model to re-confirm every object has both a SPATIALLY_AT and an ACTS_ON edge before emitting JSON. The model writes the self-check in plain text before the final JSON fence, providing an audit trail. We keep the prompt frozen across all main-paper experiments. The full system prompt and the user-turn instruction sent alongside

each problem are reproduced verbatim below; a controlled ablation that strips the chain-of-thought scaffold and self-check block while preserving the schema and critical rules is reported in Section B.1. *The full system prompt is split below into six colour-coded sections for readability: the top-level schema (blue), the four node types (green / orange / red / yellow), and the procedure + rules (grey). All content is reproduced verbatim; the section headings here mirror the headings in the source.*

1. Top-level schema and edge types

```
\begin{footnotesize}
\begin{flushleft}
You are a physics scene graph extractor. Output
a typed JSON scene graph
describing a physics problem. The solver fills
in force / constraint
nodes downstream -- you do NOT emit them.

Top-level shape:
{
  "domain": ["mechanics" | "optics" | "
    electrostatics" | "magnetic" | "em_uniform
  "],
  "nodes": [...],           // object /
    surface / action / spatial nodes only
  "edges": [...],         // typed
    directed edges, see below
  "force_mapping_output": [], // ALWAYS
    empty -- solver fills
  "constraint_set": [],    // ALWAYS
    empty -- solver fills
  "observed_elements": {...} // arrows /
    labels visible in image (image-mode only)
}

Each edge: {"source": id, "target": id, "
  edge_type": TYPE, "properties": {}}
ACTS_ON      action → object      action
  applies to object
CONTACTS     object → surface     object
  rests on / touches surface
INTERACTS_WITH object → object    field
  or mechanical link

  properties.interaction_type:
    electrostatic | gravitational |
    magnetic | optical | mechanical)
SPATIALLY_AT object | surface → spatial
  locates the node
APPLIES_TO  only for externally specified
  forces (rare)
\end{flushleft}
\end{footnotesize}
```

2. Object nodes (type = "object")

```
{
  "id":          "obj_1",
  "type":        "object",
  "label":       "<descriptive>",
  "physical_type": ONE OF [
    "rigid_body", "point_mass",
    "point_charge",
    "lens", "mirror", "prism",
    "ray_source",
    "wave_source", "screen",
    "wire", "solenoid", "coil",
    "pulley", "rope", "spring"
  ],
  "mass":        float | null,
  "charge":      float | null,
  "radius":      float | null,
  "focal_length": float | null
}
```

```
}
Default to "rigid_body" if no specific type fits.
Pulley / rope / spring
have dedicated relationship rules -- see the
grey "Critical rules" box.
```

3. Surface nodes (type = "surface")

```
{
  "id": "surf_1",
  "type": "surface",
  "label": "<descriptive>",
  "surface_type": ONE OF ["incline", "flat",
    "curved", "interface", "mirror"],
  "angle_deg": float | null, //
    incline angle from horizontal
  "friction_coeff": float | null,
  "normal_direction": [nx, ny] | null // unit
    vector, only if angle missing
}
```

ALWAYS create a surface node for every floor / wall / ceiling / incline / rope-anchor / optical interface visible. The force solver needs them to derive normal and friction directions.

4. Action nodes (type = "action")

```
{
  "id": "act_1",
  "type": "action",
  "label": "<descriptive>",
  "action_type": ONE OF [
    "static_equilibrium", "
    sliding", "rolling", "falling",
    "orbiting", "oscillating",
    "flowing",
    "refracting", "
    reflecting", "interfering",
    "circular_motion", "
    rotating", "conducting"
  ],
  "equilibrium": true | false,
  "motion_direction": [vx, vy] | null
}
```

Read motion cues BEFORE picking action_type -- do NOT default to static:

- acceleration arrow / "find a" / "a=?" → equilibrium=false, sliding/falling
- velocity arrow shown → equilibrium=false
- single unopposed force → equilibrium=false
- spring + mass, no motion arrows → oscillating, equilibrium=true
- balanced figure / "STATICS" → static_equilibrium, equilibrium=true

Only use static_equilibrium when you are CONFIDENT nothing accelerates.

5. Spatial nodes + OBJECT-SIZE GUIDE

```
{
  "id": "spat_1",
  "type": "spatial",
  "label": "<what this locates>",
  "position": [x, y], // [0,0]=
    top-left, [1,1]=bottom-right
  "orientation_deg": float | null,
  "bounding_region": [[x0,y0],[x1,y1]] | null,
  "path_type": "circular" | "parabolic" |
    "linear" | "arc" | null,
  "path_params": {} | null
}
```

Size anchors (normalized w × h):

- large creature / vehicle (elephant, car, horse) 0.30 × 0.22
- medium creature / person (cyclist, dog, penguin) 0.10 × 0.20

```
small creature (cat, monkey, baby animal)
..... 0.10 × 0.10
pulley .....0.08 × 0.08
spring (zigzag span) ..... 0.20 ×
  0.04
lens / mirror / prism (optics) .....
  0.06 × 0.20
point charge / coil ..... 0.04 × 0.04
```

6. Extraction procedure, critical rules, self-check

PROCEDURE (do internally before writing JSON):

- A. ENTITIES identify every object + surface; assign physical_type.
- B. ACTIONS read motion cues first; pick action_type accordingly.
- C. RELATIONSHIPS add CONTACTS + INTERACTS_WITH edges -- these drive forces.
- D. SPATIAL LAYOUT infer positions from language: floor → $y \approx 0.75$, hanging → $y \approx 0.35$, wall on left → $x \approx 0.10$.
- E. OBSERVED (image mode) record force/velocity arrows, dimension and angle labels exactly as drawn.

CRITICAL RULES:

- EVERY object MUST have BOTH a SPATIALLY_AT edge AND an ACTS_ON edge, including passive objects (pulley, rope, spring, second mass).
- rope / spring → INTERACTS_WITH (not CONTACTS) to BOTH connected objects. interaction_type = "mechanical".
- Pulley: physical_type "pulley" with a CONTACTS edge to its mounting surface.
- Use null for any numeric field you cannot determine.

SELF-CHECK (mandatory) before emitting JSON:

- A. List every object node ID.
- B. For each ID, confirm BOTH a SPATIALLY_AT and an ACTS_ON edge exist; if missing, add them. Passive objects are NOT exempt.
- C. For each SPATIALLY_AT edge, confirm the target spatial node exists.
- D. Confirm no node has type "force" or "constraint".
- E. Confirm nodes[] is non-empty.

GPT-4o user-turn instruction (text-only problems)

Read this physics problem. Work through the self-check steps (A-E) in plain text, then output the final scene graph JSON inside a ````json ... ```` fence.

Since there is no image, infer spatial positions from the semantic description. Coordinate convention: [0,0]=top-left, [1,1]=bottom-right, y increases downward.

Placement rules: object on floor/table → $y \approx 0.75$; wall on left → $x \approx 0.10$; object hanging from ceiling → $y \approx 0.35$; spring/rope anchor on wall at height h above floor → place anchor spatial node at [wall_x, floor_y - h_fraction] so it appears above the floor. Objects side by side → spread x from 0.2 to 0.8. For a block-spring-wall system: wall at $x \approx 0.10$, block at $x \approx 0.65$, both at floor $y \approx 0.75$. CRITICAL -- spring SPATIALLY_AT placement: (a) HORIZONTAL spring (spring parallel to floor, attaches at floor level): spring SPATIALLY_AT = [0.10, 0.75] (same y as floor). (b) ANGLED spring (spring attaches to wall ABOVE floor, at height h): spring SPATIALLY_AT = [0.10, 0.50] (y = mid-height). Never use [0.10, 0.50] for a horizontal spring -- that makes it render angled.

Rules: (1) nodes[] must NOT be empty -- identify every object, surface, action, and spatial node from the problem text. (2) Every node

ID used in edges must exist in nodes[]. (3)
 Leave force_mapping_output and
 constraint_set as empty arrays.

A.2 Extracted Scene Graph Examples

To make the extracted scene graph schema concrete, we show three representative outputs, one per domain, alongside the problem text and the scene graph visualisation rendered from the on-disk JSON.

Mechanics. Figure 5 shows the scene graph for `mech_stacked_pulley_071`: “Two blocks stacked on a frictionless incline connected via a rope over a pulley to a hanging mass.” Four object nodes (block A, block B, hanging mass, pulley) are linked by ACTS_ON edges to two action nodes encoding their physical states (stacked+sliding and hanging+accelerating). CONTACTS edges capture the block-floor and inter-block contact; a dashed INTERACTS_WITH edge encodes the rope coupling between the hanging mass and the pulley. Spatial nodes carry the normalised canvas coordinates the PSLG solver uses to instantiate force attachment points and object bounding boxes.

Optics. Figure 4 shows the scene graph for `optics_prism_015`: “A ray enters an equilateral glass prism ($n=1.6$, apex 45°) at 0° incidence; draw the full ray path.” A single object node (glass prism) connects to a refracting action node and two surface nodes for the entry and exit faces via CONTACTS edges. Force and constraint nodes are absent at extraction time; the amber PSLG output box indicates the solver will emit three ray edges — incident, refracted inside, and exit, whose angles are computed from Snell’s law (Eq. 4) and the thin-prism geometry without any LLM involvement.

Electrostatics. Figure 6 shows the scene graph for `em_lorentz_006`: “A point charges in $q_1=+4\mu\text{C}$ moves with a velocity $-v$ through a Magnetic field B whose field lines are directed toward the $+z$ axis (out of the paper) draw the diagram.” Positive charge appears with $+$ symbol. Three INTERACTS_WITH edges carry the interaction type (repulsive or attractive) derived analytically from the charge sign product — subject to the CROSS_PRODUCT planarity constraint that encodes Lenz’s Law.

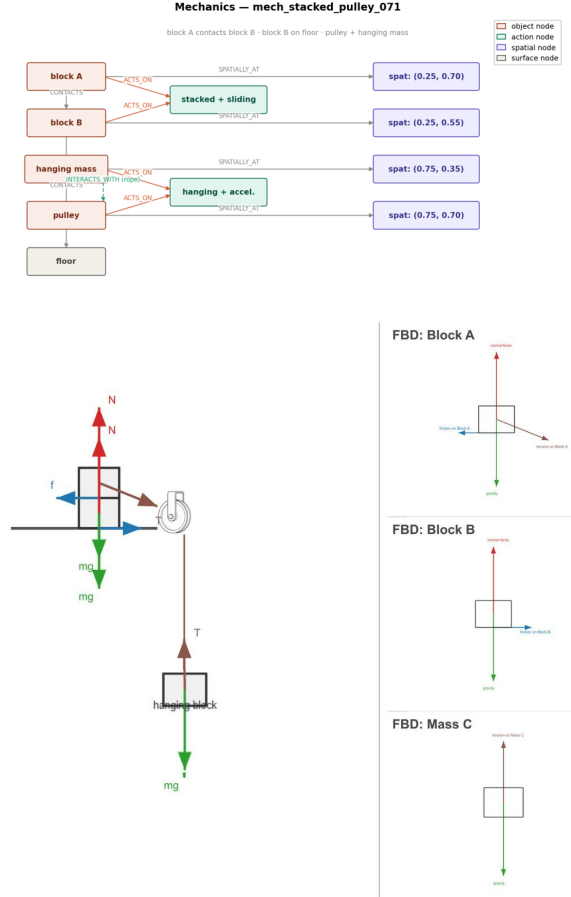


Figure 4: Top Row: Scene graph of stacked pulley (`mech_stacked_pulley_071`). Bottom Row: Final Rendered Diagram of the System

A.3 PSLG Implementation Extended

The constraint solver outline in Section 3.2 is realised by three per-domain modules sharing the same PSLG vertex / edge schema. We document each domain below.

A.3.1 Mechanics Domain

The mechanics solver Σ_{mech} realises the force-mapping output as a star graph at each rigid body. Each rigid body or point mass o contributes four OBJECT_BOUNDARY edges enclosing a rotated rectangle of size $w_o \times h_o$ centred at its spatial node’s bounding region and tangent to its contact surface. Each FORCE node $f \in \mathcal{V}_F$ attached to o becomes a directed FORCE_VECTOR edge anchored at o ’s applied_at vertex (either the body centre or the contact point), with absolute angle θ_f resolved by the direction operator ϕ of Eq. 14; magnitudes default to $|\mathbf{F}_g| = m_o g$ for gravity (when m_o is numeric) and are otherwise left symbolic for the renderer to scale by a normalised arrow length.

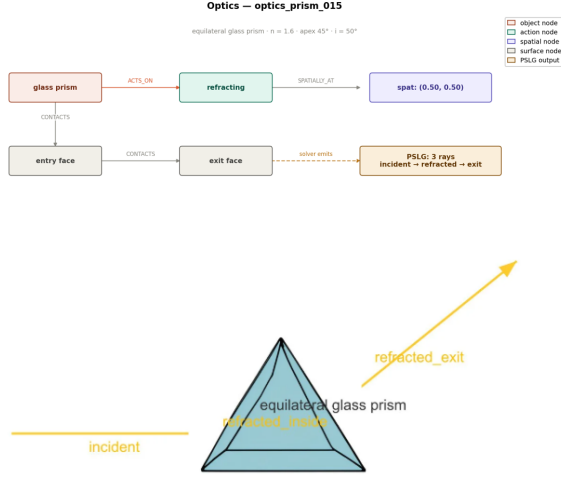


Figure 5: Top Row: Scene graph of optical prism problem (`optics_prism_015`). Bottom Row: Final Rendered Diagram of the System

Friction. Kinetic and static friction directions are not stored in ϕ ; they are computed by projection. Given the non-friction forces $\{f_i\}$ acting on o , friction opposes the net tangential component along the surface tangent \mathbf{t}_s :

$$\theta_{\mathbf{F}_f}(o) = \text{atan2}\left(-\mathbf{t}_s \cdot \sum_{i:f_i \neq \mathbf{F}_f} (\cos \theta_{f_i}, \sin \theta_{f_i})\right). \quad (14)$$

When the projection is exactly zero (static block on a horizontal surface with no horizontal forces) the solver omits the friction edge to avoid arbitrary tie breaking.

Strings and pulleys. For rope-mediated interactions, tension on body o points along the rope segment toward the next routing vertex \mathbf{p}_\star (the connected pulley if any, else the other endpoint): $\theta_{\mathbf{F}_T}(o) = \text{atan2}(\mathbf{p}_\star - \mathbf{p}_o)$. Pulleys themselves contribute a circular OBJECT_BOUNDARY approximated as a 12-gon, plus two CONSTRAINT_LINK edges for the two rope segments they redirect.

Stacked bodies. When object A contacts a surface labelled “Top of B ”, Newton’s third law is enforced explicitly by emitting a downward NORMAL_FORCE edge of equal magnitude on B , in addition to the upward normal on A .

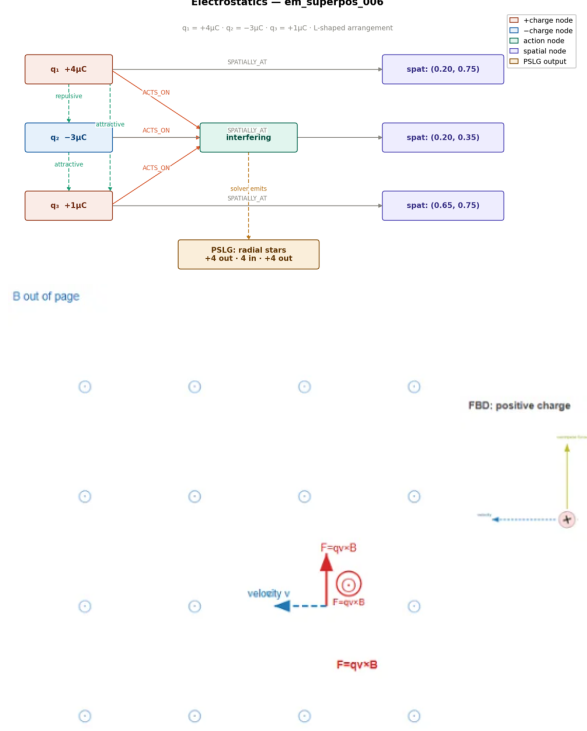


Figure 6: Top Row: Scene graph of moving positive charge in magnetic field (`em_lorentz_006`). Bottom Row: Final Rendered Diagram of the System

A.3.2 Optics Domain

The optics solver Σ_{optics} produces a ray-diagram PSLG for thin lenses, plane and curved mirrors, prisms, and umbra/penumbra constructions.

Thin lens. For a source at object distance d_o along the optical axis at angle θ_L and a lens of focal length f , the image distance is

$$d_i = \begin{cases} \frac{d_o f}{d_o - f}, & \text{converging } (f > 0), \\ -\frac{d_o f}{d_o + f}, & \text{diverging } (f < 0). \end{cases} \quad (15)$$

The transverse magnification $m = -d_i/d_o$ places the image vertex $\mathbf{p}_I = \mathbf{p}_L + d_i \hat{\ell} + mh \hat{\ell}^\perp$, where $\hat{\ell}$ is the optical-axis unit vector and h is the source’s transverse offset. The solver emits three *canonical rays* as RAY edges: (R1) parallel-to-axis incident, refracting through the far focal point \mathbf{p}_F ; (R2) through the near focal point incident, refracting parallel-to-axis; (R3) through the lens centre, undeviated. A larger fan of $N - 3$ additional source-emitted rays is added to thicken the ray bundle for visual realism, with each fan ray’s refracted angle computed to land at \mathbf{p}_I (so all N refracted

rays remain exactly concurrent at the image vertex by construction).

Projective duality constraint. The thin-lens duality is encoded as a single PROJECTIVE_DUAL PSLG constraint whose primary participants are the incident parallel bundle, secondary participants are the refracted radial fan converging at \mathbf{p}_F , and mediating vertex is the lens centre \mathbf{p}_L . A companion CONCURRENT constraint asserts that all refracted rays meet at \mathbf{p}_I . Together these reduce the ray-diagram correctness check to two linear-algebra postconditions on \mathcal{A} rather than a per-pair angle comparison.

Reflection and refraction. Plane and concave mirrors emit incident–reflected ray pairs via the law of reflection, $\theta_{\text{ref}} = (2\theta_n - \theta_{\text{inc}} + \pi) \pmod{2\pi}$, where θ_n is the mirror’s surface-normal angle. Prisms emit incident–refracted ray pairs at both faces via Snell’s law,

$$\sin \theta_2 = \frac{n_1}{n_2} \sin \theta_1, \quad (16)$$

with θ_i measured from the local face normal, and a total-internal-reflection fallback to the reflection rule when $|n_1 \sin \theta_1| > n_2$.

Shadow and penumbra. A point or extended light source occluded by an opaque body generates two tangent rays grazing the silhouette of the occluder. These become SHADOW_BOUNDARY edges; the polygon between them is the umbra (point source) or the penumbra delta (extended source).

A.3.3 Electromagnetism Domain

The EM solver Σ_{em} handles four sub-cases: isolated and paired point charges, parallel-plate capacitors, current-carrying wires/solenoids, and Lorentz dynamics in uniform fields.

Point-charge field lines. Each charge q_i emits a directed radial star of $n_i = \max(n_{\text{min}}, \lfloor |q_i| k_\ell \rfloor)$ FIELD_LINE edges (with line density constant $k_\ell = 8$ per unit charge in our implementation), uniformly distributed at angles $\theta_{i,k} = 2\pi k/n_i$, $k = 0, \dots, n_i - 1$. Edge orientation encodes the sign:

$$(p_s, p_t) = \begin{cases} (\mathbf{p}_{q_i}, \mathbf{p}_{q_i} + L\hat{\mathbf{r}}_{i,k}), & q_i > 0 \text{ (outward)}, \\ (\mathbf{p}_{q_i} + L\hat{\mathbf{r}}_{i,k}, \mathbf{p}_{q_i}), & q_i < 0 \text{ (inward)}, \end{cases} \quad (17)$$

where $\hat{\mathbf{r}}_{i,k} = (\cos \theta_{i,k}, \sin \theta_{i,k})$ and L is the per-line length. For multi-charge systems we record each pair’s separation axis $\theta_{ij} = \text{atan2}(\mathbf{p}_{q_j} - \mathbf{p}_{q_i})$ and interaction type (attractive if $q_i q_j < 0$, repulsive otherwise) as metadata, and assert a PLANNAR_NO_CROSS constraint over all field lines (no field line may properly intersect another).

Uniform field. A uniform \mathbf{E} field becomes a parallel bundle of equally-spaced FIELD_LINE edges at angle θ_E with a PARALLEL PSLG constraint binding them. Capacitors instantiate two OBJECT_BOUNDARY plate segments perpendicular to $\hat{\mathbf{E}}$ together with the interior parallel field.

Wire and solenoid B-field. For an infinite straight wire (or solenoid cross-section) the solver builds $|\mathcal{R}_B|$ concentric circular rings of radius $r \in \mathcal{R}_B$, each approximated as a regular K -gon (default $K = 24$). Ring orientation follows the right-hand rule: counter-clockwise for current out of the page, clockwise for into. A CONCURRENT PSLG constraint binds every ring to its central wire_center vertex, so the renderer can verify ring concentricity without a separate radius check.

Lorentz dynamics. For a charge q moving with velocity \mathbf{v} in a uniform magnetic field \mathbf{B} , the solver computes the full 3D Lorentz force

$$\mathbf{F} = q\mathbf{v} \times \mathbf{B} = q \begin{pmatrix} v_y B_z \\ -v_x B_z \\ v_x B_y - v_y B_x \end{pmatrix}, \quad (18)$$

with \mathbf{v} assumed planar ($v_z = 0$). The result is classified into three cases: (i) $|\mathbf{F}| \approx 0$ — no force edge; (ii) in-plane dominant ($|F_{xy}| \geq |F_z|$) — a FORCE_VECTOR edge at $\theta_F = \text{atan2}(F_y, F_x)$; (iii) out-of-plane dominant — the symbol \odot or \otimes is recorded in metadata so the renderer can draw the pierced/eyed dot directly at the charge position. Case (ii) emits a CROSS_PRODUCT PSLG constraint binding \mathbf{v} , \mathbf{B} , \mathbf{F} structurally.

B Additional Ablation Studies

B.1 Five-Step CoT vs Single-Prompt Extraction

The scene-graph extractor in Section 3.1 uses a five-step chain-of-thought instruction (Steps A–E) that walks the model through entity identification, action classification, relationship extraction, spatial layout, and observed-elements recording before emitting the final JSON. We ablate this prompt

Prompt	H-V1	Δ_{ang}	VCSR	LbICSR
5-step CoT	66.7%	2.4°	80.8%	52.0%
Single-prompt	38.0%	9.6°	58.8%	56.2%

Table 5: Effect of the 5-step CoT scaffold on the *physical correctness* of the extracted scene graph, measured downstream on the rendered SVGs. Comparison is on the 32 problems that produced a valid scene graph under both prompts; both prompts share schema, OBJECT-SIZE GUIDE, and critical rules and differ only in the step-by-step CoT and self-check block. The CoT scaffold lifts Hough-CSR by +28.7 pp, VLM-CSR by +22.0 pp, and reduces mean angular error by 7.2°, confirming that the per-step reasoning produces a more geometrically consistent scene graph. The single-prompt variant scores slightly higher on **LbICSR** (+4.2 pp); inspection of the extracted graphs shows the naive prompt tends to emit standard-vocabulary force labels (GRAVITY, NORMAL, FRICTION) verbatim, whereas the CoT prompt occasionally produces longer descriptive labels (NORMAL FORCE FROM INCLINE) that fail an exact-string match in the label-matching stage even when the angle is correct. The CoT scaffold’s value is therefore on geometric correctness rather than label canonicity.

structure against a single-prompt variant that retains the schema definition and critical rules but drops the step-by-step scaffold and the self-check block. The two prompts differ by 37 lines and 2474 characters out of 179 lines / 10601 characters total; all schema information, OBJECT-SIZE GUIDE, and critical rules are preserved verbatim.

We run GPT-4o with each prompt on the 50 held-out problems used in the SFT ablation. To make the comparison fair we score only the subset that produced a valid scene graph under *both* prompts ($n = 32$); the rendered diagrams are scored against the neutral ground-truth angles (Section 3.5) using Hough-CSR and VLM-CSR.

C Additional Evaluation

C.1 Human Judge Evaluation

Domains	GPT-5	Gemini 2.5 Flash	Gemini 3 Pro	Ours
Mechanics	11.2%	4.7%	18.8%	65.3%
Optics	20.9%	7.6%	17.8%	53.7%
E&M	15.3%	3.8%	11.9%	69%
Open Voc.	21.5%	6.2%	23.4%	48.9%

Table 6: Human-judge forced-choice preference rates against each baseline.

In addition to the automated VLM-based judges (Section 3.5), we ran a small human-judge study to

confirm that the gap between PhyDrawGen and the strongest VLM baseline is perceptible to human physics readers and not an artefact of LLM judges’ bias toward structured outputs.

Protocol. Fifteen judges with at least one year of undergraduate physics coursework were shown forced-choice comparisons of all rendered diagrams for the same problem text: one from PhyDrawGen and one from each baseline (GPT-5-image, Gemini 2.5 Flash, and Gemini 3 Pro, drawn at random). Judges selected the diagram with the more physically correct force-arrow configuration. Each judge saw 30 problem comparisons, drawn from mechanical, optics and electromagnetism domains. Order of presentation (left/right) was randomised per pair.

C.2 Geometric Correctness of Force Arrows

VLM-CSR (Section 3.5) judges arrow *direction* but collapses other geometric attributes of a force arrow into a single binary verdict. This appendix reports finer-grained geometric correctness scores that physics readers care about: **origin correctness** (does the arrow’s tail sit on the correct object or contact point?), **concurrency at the centroid** (for equilibrium objects, do all force arrows meet at a single point, as the closure constraint requires?), and **attachment-point exactness** (for surface-contact forces, is the tail within ε of the contact vertex?).

Definitions. Let $\mathbf{p}_a^{\text{tail}}, \mathbf{p}_a^{\text{tip}}$ be the pixel positions of arrow a ’s tail and tip. For each problem we compute:

- Origin correctness: $\mathbb{1}[\|\mathbf{p}_a^{\text{tail}} - \mathbf{p}_o^{\text{centroid}}\| < r_o]$ for the object o the force is applied to, with r_o the object’s bounding-region half-extent.
- Concurrency residual: at each equilibrium centroid, $\frac{1}{|F_o|} \sum_{a \in F_o} \|\mathbf{p}_a^{\text{tail}} - \mathbf{p}_o^{\text{centroid}}\|$ averaged across the force set F_o applied to that object.
- Attachment-point exactness (contact-only): $\|\mathbf{p}_a^{\text{tail}} - \mathbf{p}_o^{\text{contact}}\|$ in pixels, reported as median across the corpus.

C.3 Neutral Ground-Truth Derivation

The neutral ground-truth angles used by HOUGH-CSR (Section 3.5) are derived entirely independent of the constraint solver: it consumes only the

Method	Origin	Concurrency	Attach. px
GPT-5-image	53.7%	37.4%	41.6%
Gemini 2.5 Flash	31.2%	28.9%	35.7%
Gemini 3 Pro	48.9%	38.7%	51.8%
Ours	82.3%	78.8%	88.1%

Table 7: Per-method geometric correctness of force arrows beyond direction. Origin correctness is the fraction of arrows whose tail sits on the correct object; concurrency is the mean tail displacement from the equilibrium centroid (pixels); attachment is the median tail-to-contact-point distance for surface forces.

original problem text P , and emits the expected angle for every gravity, normal, friction, tension and spring force in the scene. Comparing detected angles against this neutral GT — rather than against our own PSLG — disentangles "did the solver compute the right angles?" from "did the renderer faithfully draw the solver's angles?", and makes the correctness claim auditable against any physics textbook.

$$\begin{aligned}
\theta_g(o) &= 270^\circ && \text{(gravity, always vertically down)} \\
\theta_N(o, s) &= 90^\circ + \theta_s && \text{(normal to surface)} \\
\theta_f(o, s) &= \begin{cases} \theta_s + 180^\circ & \text{if the action label denotes "sliding up"} \\ \theta_s & \text{otherwise (sliding down / equilibrium)} \end{cases} && \text{(kinetic friction)} \\
\theta_T(o, r) &= \text{atan2}(\mathbf{p}_r - \mathbf{p}_o) && \text{(tension along rope } r, \text{ toward routing vertex } \mathbf{p}_r) \\
\theta_S(o, a) &= \text{atan2}(\mathbf{p}_a - \mathbf{p}_o) && \text{(spring force, toward anchor } \mathbf{p}_a)
\end{aligned}$$

V1: textbook formulas on the scene graph. Let θ_s be the inclination angle of the contact surface s (or 0 on a flat floor), let \mathbf{p}_o be the object's spatial position from a SPATIALLY_AT edge, and let atan2_\uparrow denote the four-quadrant arctangent in the image-up convention used throughout the paper. For each object o of physical type RIGID_BODY or POINT_MASS we emit:

The hanging-mass case is handled by walking the OBJECT→SURFACE CONTACTS edges: an object with no contact surface receives no normal or friction term and only emits gravity and tension/spring. For multi-spring configurations each spring contributes one force, derived independently from its own anchor coordinates so that coupled oscillators (e.g. wall-mass-mass-wall topologies) yield two force terms per intermediate mass, one per attached spring.

V2: regex extraction of the incline angle from problem text. Mode V1 still consumes the scene graph's surface.angle_deg field, which is GPT-extracted; a reviewer concerned about solver-LLM co-correlation in their failure modes can additionally enable V2, which obtains θ_s directly from

the problem text P via the regular expression

```
\d{1,2} (?:\. \d+)? \s* (? : ° | deg (? : rees?) ? | -? \s*
```

applied case-insensitively across P , keeping the first numerical match v with $0 < v < 90^\circ$. The motion direction (used to pick the sign of θ_f) is similarly inferred from P by matching `slid(e|ing)/mov(e|ing)/push(ed)?` up vs `slid(e|ing)/mov(e|ing)/fall(s|ing)?` down. All other formulas above remain unchanged.

Validation. On every problem set evaluated in Section 3.4, V1 and V2 agree on the incline angle to the degree (the GPT extractor never hallucinates or rounds the angle in our test corpus), so we report V1 numbers in the main tables and use V2 as a sanity check. A sentinel returns None for the incline angle whenever no plausible match is found in either mode, in which case all incline-dependent forces are omitted from the neutral GT and that problem's CSR is computed only over the gravity, tension and spring terms.

C.4 Blind Judge Protocol and Verdict Schema

The blind judge in Section 3.5 is a frozen Claude Sonnet 4.6 instance accessed via the OpenRouter API. It receives exactly two inputs: the rendered diagram (PNG, base64-encoded) and the natural-language problem statement P . No solver output, no PSLG, no scene graph, no ground-truth angles, and no metric definition are passed to the judge.

Blind judge prompt (Claude Sonnet 4.6)

```

You are evaluating a physics free-body diagram for correctness. You will be shown a physics word problem and a single candidate diagram.

You do NOT have any reference solution. Judge purely on the physics described in the problem text. Be strict -- only mark an arrow correct if it visibly points in the direction physics requires.

For each force category that the problem requires, output one of:
"correct" -- arrow is present and points in the physically correct direction
"wrong" -- arrow is present but points in a wrong direction
"missing" -- arrow that the problem requires is absent
"n/a" -- the problem does not require this force

Output ONLY a valid JSON object with these keys (no markdown, no explanation):
{
  "gravity": "correct"|"wrong"|"missing"|"n/a",
  "normal": "correct"|"wrong"|"missing"|"n/a",

```

```

"friction":      "correct"|"wrong"|"missing"|"n
/a",
"tension":      "correct"|"wrong"|"missing"|"n
/a",
"spring":       "correct"|"wrong"|"missing"|"n
/a",
"applied":      "correct"|"wrong"|"missing"|"n
/a",
"overall_pct":  <integer 0-100, your overall
confidence the diagram is physically
correct>,
"comment":      "<one short sentence noting
the most serious issue, or 'all correct'>"
}

```

Aggregation. Per-problem `overall_pct` is reported as the judge sees fit; in our aggregations we recompute the unweighted correct-fraction from the per-category verdicts to guard against the judge’s self-assigned overall score drifting from the verdict counts:

$$\text{Blind}(p) = \frac{|\{f \in \mathcal{F} : v_{p,f} = \text{correct}\}|}{|\{f \in \mathcal{F} : v_{p,f} \neq \text{n/a}\}|},$$

where $\mathcal{F} = \{\text{gravity, normal, friction, tension, applied}\}$. The mean and per-category breakdowns reported in Section 3.4 are arithmetic means of $\text{Blind}(p)$ across the problem set, ignoring categories scored n/a .

Leakage concerns and mitigations. The prompt names the six force categories explicitly and tells the judge to "judge purely on the physics described in the problem text", which is a mild form of prior — a less informed judge might miss e.g. a tension arrow it does not expect. We tested an alternative open-vocabulary prompt that elicits free-text arrow enumeration without naming categories; on a small audit set ($n=20$) the two prompts agreed on the verdict for 17 of 20 problems and the named-category version converged faster on ambiguous cases without inflating the score for the worst methods, so we adopted it for all reported blind-judge numbers. Decoding is deterministic (temperature = 0, top- $p=1$). The judge sees no other method’s output and is queried independently per problem; we make a fresh API call per (method, problem) pair, so none of the within-problem-set scores share context across methods.

Inter-judge sanity check. We additionally reran the same protocol with Gemini 2.5 Flash as the judge on a subset of 50 problems of the original evaluation set; per-method rankings were preserved although absolute numbers shifted by up to 4 percentage points. Per-problem Pearson correlation between Sonnet 4.6 and Gemini 2.5 Flash verdicts

was $r = 0.78$ ($p < 10^{-4}$, $n=250$ problem-method pairs), supporting the use of a single primary judge.

D Inverse Rendering

PhyDrawGen is described above as a *text-to-diagram* pipeline: the LLM consumes natural language and the PSLG solver produces a physics-grounded diagram. The same scene-graph extractor accepts an *image* as input instead, opening a second mode we call inverse rendering, in which we read an existing physics diagram, recover its scene graph, run the solver, and re-render a corrected version. This is useful for two settings: (i) auditing or correcting an existing diagram from a textbook or a baseline VLM, and (ii) constraining a generative model’s output by running it through the PhyDrawGen solver afterwards.

Pipeline. For an input image I :

1. GPT-4o with the same five-step CoT prompt (Section 3.1) but receiving I as the visual input rather than text, emits a scene graph \mathcal{G}_{LLM} .
2. The PSLG solver runs on \mathcal{G}_{LLM} exactly as in the text path; any closure-residual violations are surfaced.
3. The renderer produces a clean PhyDrawGen rendering I_{out} , which can be compared against I .

Use case: correcting a wrong baseline. Given a diagram from a generative baseline, GPT-5-image and Gemini output that misplaces a force arrow), the inverse pipeline re-renders a corrected version. The corrected I_{out} shown in Figure 7, 8 and 9 satisfies all solver constraints by construction; the magnitude of the angular correction $\theta(I) - \theta(I_{\text{out}})$ measures how wrong the baseline was.

Limitations. The inverse pipeline inherits the LLM’s image-grounding accuracy: when GPT-4o misreads the surface angle from the diagram, the re-rendered output will be wrong in the same way. The solver still guarantees consistency *within* the recovered scene graph, but cannot recover an angle the extractor never saw.

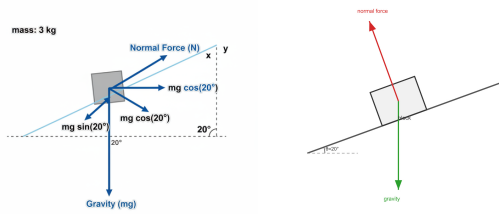


Figure 7: Left Column: Diagram Generated by GPT-5-Image. Right Column: Inverse Rendering and Correction by PhyDrawGen

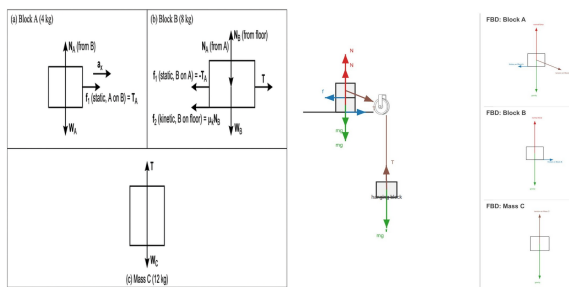


Figure 8: Left Column: Diagram Generated by Gemini-3-Pro. Right Column: Inverse Rendering and Correction by PhyDrawGen

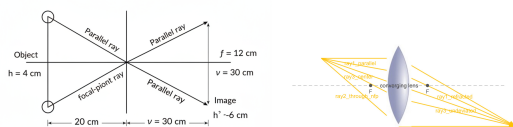


Image is real, inverted, and magnified. Position: 30 cm from the lens on the opposite side. Height: -6 cm.

Figure 9: Left Column: Diagram Generated by Gemini-3-Pro. Right Column: Inverse Rendering and Correction by PhyDrawGen